

Article

Properties of Carbon Fibers as Supercapacitor Electrodes via Electrospinning Using a Blending Solution of Polyacrylonitrile and Bisphenol A

Ji-Woo Park ¹ and Young-Wan Ju ^{1,2,*}

¹ Department of Chemical Engineering, College of Engineering, Wonkwang University, Iksan 54538, Jeonbuk, Republic of Korea; wldnro4612@naver.com

² ICT Fusion Green Energy Research Institute, Wonkwang University, Iksan 54538, Jeonbuk, Republic of Korea

* Correspondence: ywju1978@wku.ac.kr

Abstract: Supercapacitors have attracted attention as efficient energy storage systems owing to their high power density and cycling stability. The use of appropriate electrode materials is important for high-performance supercapacitors, and various carbon materials have been studied as supercapacitor electrodes. In this study, carbon nanofibers with high specific surface areas were fabricated via a simple electrospinning process. Carbon nanofibers were fabricated by adjusting the ratio of polyacrylonitrile (PAN) to bisphenol A (BPA) and evaluated as electrode materials for supercapacitors. With the addition of BPA, improved specific surface area and oxygen functional groups were observed compared with nanofibers using only PAN. Therefore, BPA3, which had the highest specific surface area, exhibited a 28% improvement in capacitance (162 F/g) compared with BPA0 fabricated using only PAN. Carbon nanofibers fabricated by adjusting the ratio of BPA to PAN are promising electrodes for supercapacitors owing to their high capacitance and stability.

Keywords: blending solution; carbon nanofibers; electrospinning; oxygen functional group; supercapacitor



Citation: Park, J.-W.; Ju, Y.-W. Properties of Carbon Fibers as Supercapacitor Electrodes via Electrospinning Using a Blending Solution of Polyacrylonitrile and Bisphenol A. *Energies* **2024**, *17*, 1732. <https://doi.org/10.3390/en17071732>

Academic Editors: Kumaran VEDIAPPAN, Chenrayan Senthil and Baskaran Rangasamy

Received: 5 March 2024

Revised: 1 April 2024

Accepted: 2 April 2024

Published: 4 April 2024



Copyright: © 2024 by the authors. Licensee MDPI, Basel, Switzerland. This article is an open access article distributed under the terms and conditions of the Creative Commons Attribution (CC BY) license (<https://creativecommons.org/licenses/by/4.0/>).

1. Introduction

Eco-friendly energy is attracting attention to solve environmental problems of concern. Energy produced from eco-friendly energy has low efficiency if it is not used immediately [1–3]. Therefore, to utilize energy efficiently, the development of technologies for converting and storing the produced energy is important [4,5]. To store electrical energy, electrochemical devices such as lithium-ion batteries and supercapacitors are used as energy storage systems [6]. Among them, supercapacitors are attracting attention in application fields such as transportation, home appliances, and energy due to their high power density, long cycle life, fast charge/discharge characteristics, and environmental friendliness [7–10].

Depending on the charge storage/release mechanism, supercapacitors are classified into pseudocapacitors (PCs), which store charges using the Faraday reaction, and electrochemical double-layer capacitors (EDLCs), which store charges due to the electric double layer at the interface between the electrode and electrolyte [11–13]. PCs mostly exhibit higher capacitance than EDLCs but have the disadvantages of low cycle stability and large internal resistance due to metal oxide electrodes [14–16]. On the other hand, EDLCs mainly use carbon materials such as carbon nanotubes [17–19], graphene [20–22], activated carbon [23–25], and carbon nanofibers [26–29], and are attracting attention as a promising energy storage device due to their advantages such as high energy efficiency, excellent cycle stability, nontoxicity of the material, and low cost [30,31] (Table 1).

The performance of EDLCs is influenced by the properties of the electrode material, such as active specific surface area, porosity, and surface functional groups, and many researchers are focusing on developing carbon electrode materials with these properties [22,32–34]. Among

carbon materials, carbon nanofibers fabricated via electrospinning are reported to be promising as supercapacitor electrodes due to their chemical stability, porous structure, and low processing costs [35,36]. Currently, carbon nanofibers fabricated using polyacrylonitrile (PAN) carbon precursors are widely used due to their high carbon yield and electrospinning efficiency, but their dense structure and low specific surface area result in low capacitor performance [37–39]. Therefore, to improve the low performance of carbon nanofibers, much research is being conducted to improve the pore size and porosity properties of carbon nanofibers by performing an activation process or blending them with other carbon precursor polymers [40–42].

Bisphenol A (BPA) is used in the production of carbon materials and is known to contribute to the activation process and improve specific surface area and pore properties [43]. In addition, the ring structure and oxygen functional group of BPA have structural properties that allow them to interact with other carbon materials, so they are adsorbed on the ends or planes of carbon materials and contribute to changes in the properties of blended carbon materials, making them suitable as polymers for producing carbon nanofibers [44,45]. Carbon nanofibers fabricated from these blended polymers affect their shape and pore properties due to thermal stability and chemical interactions between the blending solutions during the heat treatment process [46]. Additionally, it has the advantage of contributing to improving capacitor performance by changing its properties due to physical interactions such as dissolution, rearrangement, and swelling [47].

In this study, carbon nanofibers were fabricated via electrospinning using a blended solution of PAN and BPA. The properties of the carbon nanofibers prepared by adjusting the BPA ratio were confirmed, and their capacitor performance was evaluated using them as electrodes for EDLCs. The blended fiber with BPA had a higher specific surface area than that of the carbon nanofiber using only PAN, and the micropores and mesopores were well developed. BPA5 formed beads because of its low viscosity, confirming that BPA3 was the optimal BPA blending ratio. BPA3 exhibited excellent electrochemical performance with many oxygen functional groups, a high specific surface area, and high capacitance. In addition, excellent stability was confirmed owing to a low reduction rate of 3.2%, even after 2000 cycles, indicating that BPA3 is promising as a supercapacitor electrode.

Table 1. Comparison of capacitance of various carbon materials as electrodes.

Material	Electrolyte	C (F/g)	Cycle Stability	Ref.
Carbon nanotubes	6 M KOH (aq.)	56.04	85.4% (10,000 cycle)	[48]
Graphene	6 M KOH (aq.)	180	79.6% (4000 cycle)	[49]
Activated carbon	PVA/IL/H ₃ PO ₄ (s)	106	95% (3000 cycle)	[50]
Carbon nanofibers	2 M KOH (aq.)	155	91% (5000 cycle)	[51]
BPA3	6 M KOH (aq.)	176	96.8% (2000 cycle)	This work

2. Experimental

2.1. Materials

PAN ($M_w = 150,000$) was obtained from Sigma-Aldrich (St. Louis, MO, USA) and BPA (98%) was purchased from Samchun (Pyeongtaek, Republic of Korea). N,N-Dimethylformamide (DMF, 99.5%) was purchased from Daejung (Siheung, Republic of Korea).

2.2. Preparation of Carbon Nanofibers via Electrospinning

The 10 wt.% PAN and 10 wt.% BPA solutions were prepared using DMF as a solvent and stirred in an oil bath for 10 h. Afterwards, the dissolved solution was blended with PAN/BPA in wt.% ratios of 10:0, 9:1, 7:3, and 5:5. After sufficient stirring, carbon nanofibers were fabricated via electrospinning. Electrospinning was performed under the same conditions: an applied voltage of 20 kV, a tip/collector distance of 18 cm, and a solution supply rate of 1 mL/h. The fabricated nanofibers went through a stabilization process in an air atmosphere at 250 °C for 1 h (heating rate: 1 °C/min). The stabilized fibers were

carbonized for 2 h by heating to 800 °C at a heating rate of 200 °C/h in N₂ atmosphere and were activated by supplying CO₂ at 800 °C for 1 h.

Carbon nanofibers fabricated from a PAN/BPA blended solution were named BPA0, BPA1, BPA3, and BPA5, depending on the BPA content.

2.3. Characterization

The crystal structures of the fabricated carbon nanofibers were evaluated by X-ray diffraction (XRD, MiniFlex 600, Rigaku, Japan). XRD analysis was performed in the range of 10–80° using Cu-K α radiation in the 2-theta range. The morphology of the carbon nanofibers was observed by field-emission scanning electron microscopy (FE-SEM, S-4800, Hitachi, Japan). The Brunauer–Emmett–Teller equation (BELSORP-mini II, MicrotracBEL, Osaka, Japan) was used to determine the specific surface area, pore size, and pore volume from the N₂ adsorption/desorption isotherms measured at 77 K. The chemical components of the samples were determined using X-ray photoelectron spectroscopy (XPS, Thermo ESCALAB 250, Thermo Fisher, Waltham, MA, USA). XPS measurement was analyzed via the binding energy of C 1s using Al-K α radiation. The thermal decomposition-related properties of the samples were analyzed by thermogravimetric analysis (TGA, TGA 8000, PerkinElmer, Waltham, MA, USA) in the range of 30–1000 °C (10 °C/min) in a N₂ atmosphere.

2.4. Electrochemical Test

Galvanostatic charge/discharge (GCD) measurements and electrochemical impedance spectroscopy (EIS) were conducted using a battery testing system (BCS-815, Bio-logic, Göttingen, Germany) to analyze the electrochemical performance. The synthesized carbon nanofiber web was used as an electrode without binder, the electrode area was 1 cm², and the average mass of the loaded carbon nanofiber web was 1.2 mg. The electrochemical performance was evaluated by placing a nanofiber web electrode on a nickel foil as the current collector. Electrochemical evaluation was performed in 6 M KOH aqueous solution, and GCD was measured in the voltage range of 0–0.9 V at a current density of 1 mA/cm². EIS was performed in the frequency range of 10–100 kHz. The cell capacitance was calculated using the following equation:

$$C = (I \cdot \Delta t) / (m \cdot \Delta V)$$

where C (F/g) is the specific capacitance, I (mA) is the discharge current, Δt (s) is the discharging time, m is the mass of the electrode web, and ΔV is the discharging voltage.

3. Results and Discussion

Figure 1 shows the crystal structure of the nanofibers fabricated via electrospinning. All carbon nanofibers exhibit a broad and weak amorphous carbon peak in the range of 20–28°. The XRD pattern located at 20–28° corresponds to the (002) crystal plane of turbostratic carbonaceous substances, and pure carbon nanofibers are confirmed to be synthesized without any impurities [52]. Through the XRD analysis, no significant differences were observed with the increasing BPA ratio. However, as the BPA ratio increases, the viscosity of the blending solution decreases, indicating a slight broadening of the amorphous peak.

Figure 2 shows the morphology of the blended fibers fabricated using FE-SEM analysis. The diameters of the electrospun fibers range from 400 to 1000 nm with an average diameter of 900 nm (Figure 2a–d). Samples other than the BPA5 sample do not contain beads; however, in the case of BPA5, irregularly shaped fibers and beads are observed (Figure 2d). Beads are visible because the viscosity of the blending solution used for electrospinning decreases as the BPA ratio increases. In low-viscosity solutions under the same electrospinning conditions, a bead structure is formed at the tip owing to low molecular attraction. The formed bead-shaped jet moves to the collector without breaking, resulting in the presence of beads in the fibers [53,54]. Figure 2e–h show the SEM images of the activated carbon nanofibers according to the BPA ratio. The diameters of the activated fibers range from 150 to 700 nm, with an average diameter of 250 nm. BPA0 using only

PAN shows a smooth surface; however, the samples, except BPA0, show rough surfaces with bends and wrinkles. These surface properties result from physical processes, such as swelling, shrinking, and dissolution, that occur between the PAN and BPA layers during activation [55].

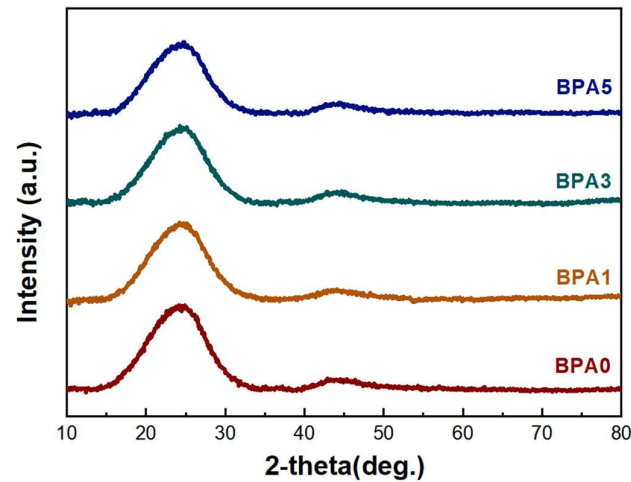


Figure 1. XRD patterns of BPA0, BPA1, BPA3, and BPA5.

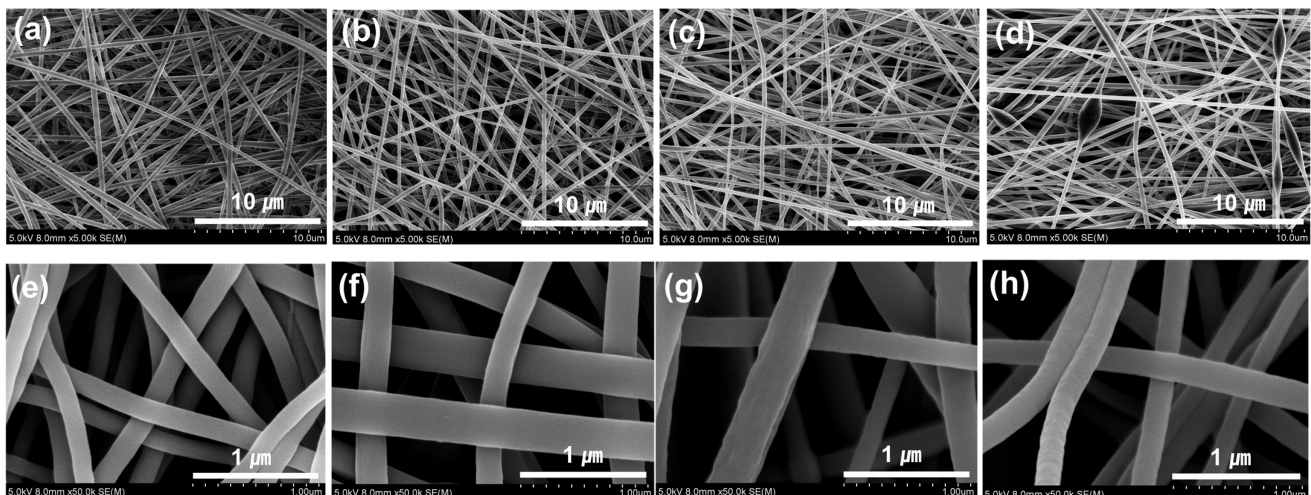


Figure 2. FE-SEM images of electrospun fiber (a) BPA0, (b) BPA1, (c) BPA3, and (d) BPA5; and of activated fiber (e) BPA0, (f) BPA1, (g) BPA3, and (h) BPA5.

To confirm the specific surface areas and pore properties of the blended fibers according to the BPA ratio, nitrogen adsorption/desorption isotherms were plotted (Figure 3). As shown in Figure 3a, BPA0 used only with PAN shows a sharp increase at a relatively low pressure with a type I curve, indicating micropore development. However, except for BPA0, BPA1, BPA3, and BPA5 exhibit type-IV curves, indicating the development of micropores and mesopores. The specific surface areas of BPA0, BPA1, BPA3, and BPA5 are 761, 875, 1053, and 924 m^2/g , respectively. As shown in Table 2, which summarizes the specific surface area and pore properties, the specific surface area and pore volume increase in proportion to the BPA ratio. However, BPA5 has a lower specific surface area and smaller pore volume compared with BPA3 owing to its bead structure. Additionally, BPA1, BPA3, and BPA5 containing BPA exhibit higher specific surface area values than BPA0. Figure 3b shows the pore-size distributions of the samples according to the BJH method. BPA0 shows well-developed micropores with diameters of 3 nm or less, and all the samples containing BPA show well-developed micropores and mesopores in the diameter

range of 2–50 nm. This confirms that changes occur between the PAN and BPA layers during the activation process following the addition of BPA, affecting the specific surface area and pore development.

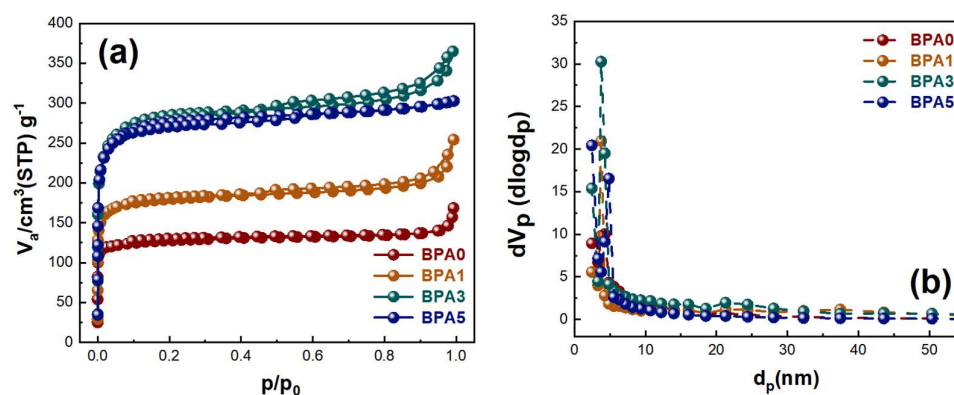


Figure 3. (a) Nitrogen adsorption/desorption isotherms of samples at 77 K, (b) Barrett-Joyner-Halenda (BJH) pore distribution.

Table 2. The summary of specific surface area and pore properties of samples.

Sample	Specific Surface Area [m ² /g]	Total Pore Volume [cm ³ /g]	Mean Pore Diameter [nm]
BPA0	761	0.368	2.12
BPA1	875	0.399	2.22
BPA3	1053	0.498	3.65
BPA5	924	0.435	2.57

TGA was performed to determine the thermal stability characteristics (Figure 4). To measure the change in weight while the sample was decomposed, according to the temperature when heat was applied, TGA analysis was performed in a N₂ atmosphere to prevent oxidation due to the reaction with O₂. As shown in Figure 4, weight loss for all samples begins around 300–400 °C. Subsequently, the weight of the sample decreases, and the residual ratios of BPA0, BPA1, BPA3, and BPA5 are 32, 41, 42, and 20%, respectively. Thus, it is confirmed that BPA1 and BPA3 have similar thermal stability characteristics and their residual contents are higher than that of BPA0, indicating that the ring structure of BPA contributes to the blended fiber between PAN and BPA. However, BPA5 is less stable during heat treatment than BPA0, which indicates that the BPA content is considerably high and that as the temperature increases, BPA decomposes thermally and does not contribute to the blended fiber between PAN and BPA.

XPS was performed to confirm the elemental composition of the sample surface after the addition of BPA. Table 3 shows the surface atomic percentages of the samples calculated using the XPS measurements. As the BPA ratio increases, the carbon and nitrogen contents decrease, whereas the oxygen content increases. This is because the atomic percentage of oxygen increases with the BPA content owing to the presence of oxygen in BPA. Figure 5 shows the C 1s spectrum of the carbon nanofibers with the addition of BPA. In the C 1s spectra shown in Figure 5a–d, C=C, C–C or C–N, and C–O or C–OH bonds appear at approximately 284.5, 285.8, and 287.5 eV, respectively. A slight shift is observed in the measured peaks for each sample. The C–C/C–O ratios of BPA0, BPA1, BPA3, and BPA5 are 1.84, 1.28, 1.08, and 1.54, respectively. For BPA1 and BPA3, the C–C/C–O ratio decreases as the BPA ratio increases, which is consistent with the contribution of BPA having a ring structure and oxygen functional groups between the PAN layers, as confirmed by the TGA curve. However, in the case of BPA5, the C–C/C–O ratio increases compared with those of BPA1 and BPA3. As confirmed by the TGA analysis, BPA5 has a high BPA content,

which is consistent with the fact that BPA is decomposed during carbonization, and the oxygen functional group and ring structure are unable to contribute between the PAN layers, thereby reducing the residual carbon content. Additionally, a wettability test based on the presence of oxygen functional groups, by measuring the contact angle, is presented in the Supporting Data. As shown in Figure S1, BPA0, BPA1, BPA3, and BPA5 exhibit contact angles of 28.2, 25.6, 22.6, and 31.5°, respectively. The wettability is proportional to the ratio of oxygen functional groups, and BPA3 exhibits good wettability. In addition, the presence of these oxygen functional groups increases the wettability between the electrode and the electrolyte and is suggested to be a factor that increases the capacitance [56].

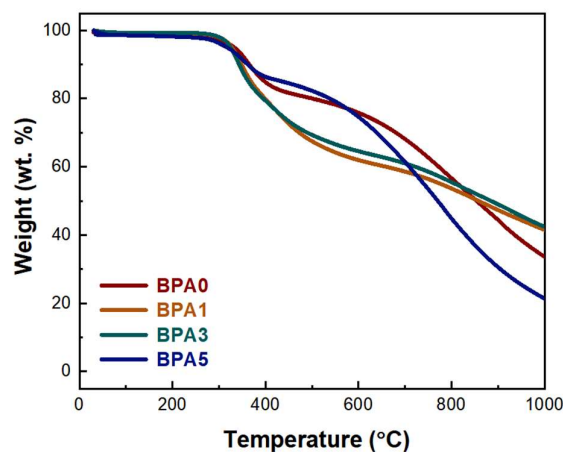


Figure 4. TGA curves of BPA0, BPA1, BPA3, and BPA5.

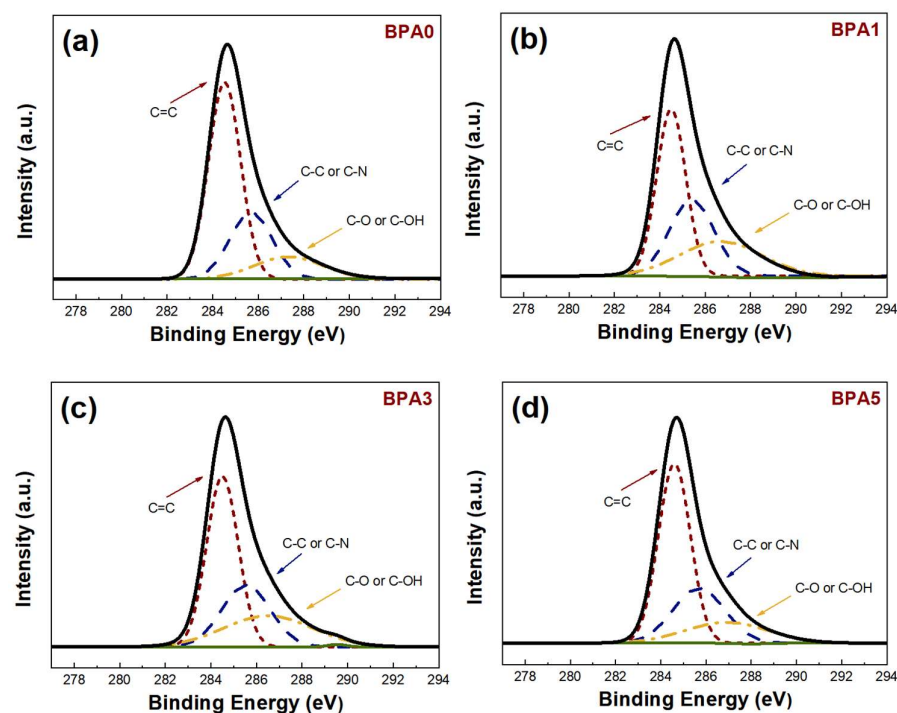


Figure 5. XPS spectra of C 1s of (a) BPA0, (b) BPA1, (c) BPA3, and (d) BPA5.

Table 3. Elemental surface composition determined through XPS analysis.

Sample	Carbon (at. %)	Oxygen (at. %)	Nitrogen (at. %)
BPA0	82.29	11.04	6.67
BPA1	81.81	12.64	5.55
BPA3	78.97	16.37	4.66
BPA5	79.98	13.99	6.03

The electrochemical performances of the blended fibers were evaluated using GCD and EIS analyses (Figure 6). The capacitance of the electrode was evaluated at a constant current density of 1 mA/cm^2 and a constant voltage of 0.9 V . As shown in Figure 6a, as the BPA ratio increases, the discharge time also increases. The capacitances of BPA0, BPA1, BPA3, and BPA5 calculated from the discharge curves (Figure 6a) and measured at a current density of 1 mA/cm^2 are 127, 135, 162, and 142 F/g , respectively. It is confirmed that BPA3 exhibits a high capacitance and improved performance by 28% compared with BPA0 using only PAN. Increases in the average pore diameter, specific surface area, and number of functional groups promote the formation of an electric double layer and improve the capacitance. However, BPA5 exhibits a lower capacitance than that of BPA3 because of its lower specific surface area and pore size owing to the presence of beads. The IR drops of the samples are shown in Figure 6a. The IR drop values for BPA0, BPA1, BPA3, and BPA5 are 0.104 , 0.091 , 0.045 , and 0.064 V , respectively. Among them, BPA3 is associated with low resistance and high conductivity of the electrode material owing to its low IR drop [57]. To analyze the changes in the electrical conductivity and resistance depending on the blended fiber, EIS measurements were performed. As shown in Figure 6b, in the high-frequency region, a semicircle is observed, which represents the internal resistance (R_S) and charge transfer resistance (R_{CT}) at the interface between the electrolyte and the carbon nanofiber web used as the electrode. The sloping curve in the low-frequency region illustrates the mass transfer at the electrode [58]. R_S values of the samples are similar in the range of 0.26 – 0.3Ω , and R_{CT} values of BPA0, BPA1, BPA3, and BPA5 are 1.344 , 0.713 , 0.244 , and 0.436Ω , respectively. BPA3 has the lowest R_S and R_{CT} values of 0.26 and 0.244Ω , respectively. A low R_S indicates a low resistance and high conductivity of the electrode materials, and a low R_{CT} value occurs because the active interface between the electrode surface and electrolyte increases owing to improved wettability [59].

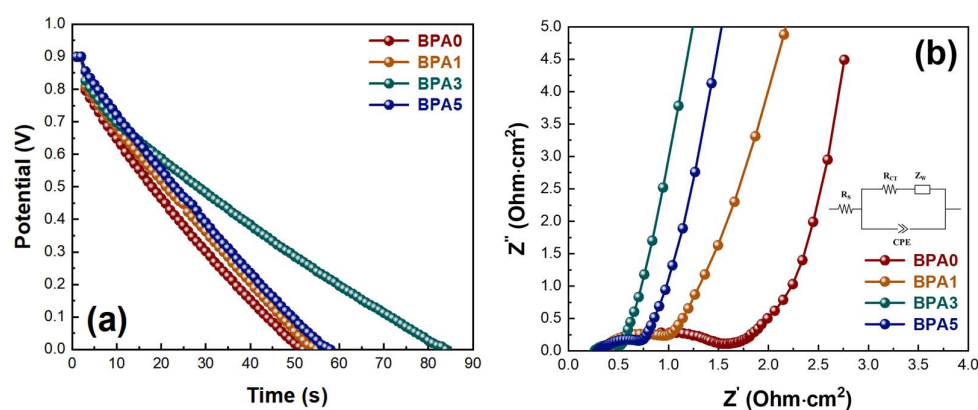
**Figure 6.** (a) Discharge curve of GCD curve of samples and (b) EIS spectra.

Figure 7a shows the change in the specific capacitance with the current density ranging from 1 to 10 mA/cm^2 . As the current density increases, the specific capacitance decreases. Relatively large hydration ions prevent access to the pore surface at high current densities, thereby reducing the specific capacitance [60]. The specific capacitance of BPA0 at 10 mA/cm^2 is reduced by approximately 18% compared with that at 1 mA/cm^2 . However, the specific capacitance at 10 mA/cm^2 for BPA3 is approximately 10% lower than that at 1 mA/cm^2 . To evaluate the stability of the blended fibers as capacitor electrodes, Figure 7b

shows the change in the specific capacitance according to the number of cycles. For all samples, the specific capacitance is almost constant as the number of cycles increases to 2000. After 2000 cycles, BPA0, BPA1, BPA3, and BPA5 exhibit reduction rates of 4.2, 3.7, 3.2, and 4.7%, respectively. BPA3 shows the lowest reduction rate and is highly stable in tests involving charge and discharge cycles. The cycle stability is consistent with the wettability confirmed through the contact angle test, shown in Figure S1, and shows improved stability owing to the excellent electrolyte permeability obtained as a result of wettability. Good cycling stability is an essential element of high-performance supercapacitors. Owing to its high specific surface area and the presence of oxygen functional groups, the cycling stability of BPA3 is improved, making it a suitable supercapacitor electrode material.

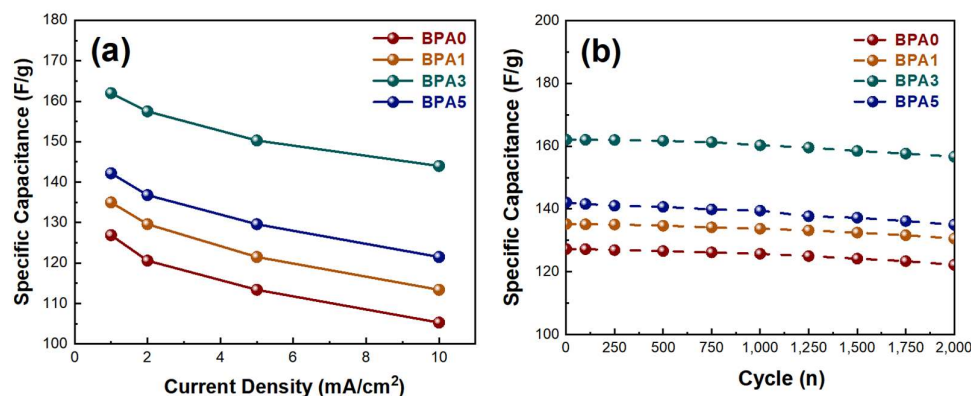


Figure 7. (a) Capacitance according to current density 1–10 mA/cm² and (b) cycle stability test of the samples.

4. Conclusions

In this study, PAN and BPA were blended in various proportions and carbon nanofibers were fabricated via electrospinning. The activated carbon nanofibers were fabricated via stabilization, carbonization, and activation after electrospinning. Compared with carbon nanofibers fabricated using only PAN, the BPA-blended fibers exhibited higher specific surface areas and larger pore volumes owing to processes such as swelling, shrinkage, or dissolution that occurred between the PAN and BPA layers during the activation process. However, BPA5 had a lower specific surface area than that of BPA3 owing to the formation of beads because of its low viscosity owing to the high BPA addition ratio. Additionally, because of the blending of BPA, the ratio of oxygen to carbon increased owing to the presence of oxygen functional groups in BPA. BPA3 exhibited a high capacitance of 162 F/g owing to its high specific surface area, oxygen functional groups, and the development of micropores and mesopores, which showed a 28% improvement in performance over that of BPA0 using only PAN. In addition, all samples exhibited excellent stability even after 2000 cycles; however, excellent cycle stability was also confirmed for BPA3, with a low reduction rate of 3.2%. Therefore, BPA3 is suitable and promising as a supercapacitor electrode due to its high capacitance and excellent cycle stability, which are required for supercapacitor electrodes.

Supplementary Materials: The following supporting information can be downloaded at <https://www.mdpi.com/article/10.3390/en17071732/s1>, Figure S1: Contact angle images of samples (a) BPA0, (b) BPA1, (c) BPA3, and (d) BPA5.

Author Contributions: Writing—original draft, J.-W.P.; writing—review and editing, Y.-W.J. All authors have read and agreed to the published version of the manuscript.

Funding: This research was supported by Wonkwang University in 2023.

Data Availability Statement: The article includes the original contributions presented in the study. Further inquiries can be directed to the corresponding author.

Conflicts of Interest: The authors declare that they have no personal relationships or competing financial interests influencing this article.

References

1. Luo, B.; Wang, B.; Li, X.; Jia, Y.; Liang, M.; Zhi, L. Graphene-Confined Sn Nanosheets with Enhanced Lithium Storage Capability. *Adv. Mater.* **2012**, *24*, 3538–3543. [[CrossRef](#)]
2. Chu, S.; Majumdar, A. Opportunities and challenges for a sustainable energy future. *Nature* **2012**, *488*, 294–303. [[CrossRef](#)]
3. Arico, A.S.; Bruce, P.; Scrosati, B.; Tarascon, J.A.; Schalkwijk, W. Nanostructured materials for advanced energy conversion and storage devices. *Nat. Mater.* **2005**, *4*, 366–377. [[CrossRef](#)]
4. Lemian, D.; Bode, F. Battery-Supercapacitor Energy Storage Systems for Electrical Vehicles: A Review. *Energies* **2022**, *15*, 5683. [[CrossRef](#)]
5. Mahapatra, A.; Mandal, M.; Mahapatra, A.D.; Anilkumar, V.; Nawrocki, J.; Chavan, R.D.; Yadav, P.; Prochowicz, D. Mechanochemically-Assisted Synthesis of 3D, 2D and quasi 2d Lead Halide Perovskites for Supercapacitor Application. *Mater. Adv.* **2024**. [[CrossRef](#)]
6. Burke, A. Ultracapacitors: Why, how and where is the technology. *J. Power Sources* **2000**, *91*, 37–50. [[CrossRef](#)]
7. Miller, J.R.; Simon, P. Electrochemical Capacitors for Energy Management. *Science* **2008**, *321*, 651–652. [[CrossRef](#)]
8. Frachowiak, E. Carbon materials for supercapacitor application. *Phys. Chem. Chem. Phys.* **2007**, *9*, 1774–1785. [[CrossRef](#)]
9. Fayon, P.; Thomas, J.M.H.; Trewin, A. Structure and Properties of a Nanoporous Supercapacitor. *J. Phys. Chem. C* **2016**, *120*, 25880–25891. [[CrossRef](#)]
10. Portet, C.; Taberna, P.L.; Simon, P.; Flahaut, E.; Laberty-Robert, C. High power density electrodes for Carbon supercapacitor applications. *Electrochimica* **2005**, *50*, 4174–4181. [[CrossRef](#)]
11. Brousse, T.; Crosnier, O.; Bélanger, D.; Long, J.W. Capacitive and Pseudocapacitive Electrodes for Electrochemical Capacitors and Hybrid Devices. In *Metal Oxides in Supercapacitors*; Elsevier: Amsterdam, The Netherlands, 2017; pp. 1–24.
12. Ning, P.; Duan, X.; Ju, X.; Lin, X.; Tong, X.; Pan, X.; Wang, T.; Li, Q. Facile synthesis of carbon nanofibers/MnO₂ nanosheets as high-performance electrodes for asymmetric supercapacitors. *Electrochim. Acta* **2016**, *210*, 754–761. [[CrossRef](#)]
13. Sun, Y.; Guo, S.; Li, W.; Pan, J.; Fernandez, C.; Senthil, R.A.; Sun, X. A green and template-free synthesis process of superior carbon material with ellipsoidal structure as enhanced material for supercapacitors. *J. Power Sources* **2018**, *405*, 80–88. [[CrossRef](#)]
14. Lim, E.; Jo, C.; Lee, J. A mini review of designed mesoporous materials for energy-storage applications: From electric double-layer capacitors to hybrid supercapacitors. *Nanoscale* **2016**, *8*, 7827–7833. [[CrossRef](#)] [[PubMed](#)]
15. Sugimoto, W.; Makino, S.; Mukai, R.; Tatsumi, Y.; Fukuda, K.; Takasu, Y.; Yamauchi, Y. Synthesis of ordered mesoporous ruthenium by lyotropic liquid crystals and its electrochemical conversion to mesoporous ruthenium oxide with high surface area. *J. Power Sources* **2012**, *204*, 244–248. [[CrossRef](#)]
16. Conway, B.E. Transition from “supercapacitor” to “battery” behavior in electrochemical energy storage. *J. Electrochem. Soc.* **1991**, *138*, 1539. [[CrossRef](#)]
17. Qu, D.; Shi, H. Studies of activated carbons used in double-layer capacitors. *J. Power Sources* **1998**, *74*, 99–107. [[CrossRef](#)]
18. Pan, H.; Li, J.; Feng, Y. Carbon nanotubes for supercapacitor. *Nanoscale Res. Lett.* **2010**, *5*, 654–668. [[CrossRef](#)]
19. Mandal, M.; Subudhi, S.; Alam, I.; Subramanyam, B.V.R.S.; Patra, S.; Das, S.; Raiguru, J.; Mahapatra, A.; Mahanandia, P. Simple and Cost-Effective Synthesis of Activated Carbon Anchored by Functionalized Multiwalled Carbon Nanotubes for High-Performance Supercapacitor Electrodes with High Energy Density and Power Density. *J. Electron. Mater.* **2021**, *50*, 2879–2889. [[CrossRef](#)]
20. Yang, W.; Ni, M.; Ren, X.; Tian, Y.; Li, N.; Su, Y.; Zhang, X. Graphene in supercapacitor applications. *Curr. Opin. Colloid Interface Sci.* **2015**, *20*, 416–428. [[CrossRef](#)]
21. Miller, J.R.; Outlaw, R.A.; Holloway, B.C. Graphene electric double layer capacitor with ultra-high-power performance. *Electrochim. Acta* **2011**, *56*, 10443–10449. [[CrossRef](#)]
22. Bornstein, A.; Hanna, O.; Attias, R.; Luski, S.; Brousse, T.; Aurbach, D. Carbon-based composite materials for supercapacitor electrodes: A review. *J. Mater. Chem. A* **2017**, *5*, 12653–12672. [[CrossRef](#)]
23. Wu, F.C.; Tseng, R.L.; Hu, C.C.; Wang, C.C. Effects of pore structure and electrolyte on the capacitive characteristics of steam-and KOH-activated carbons for supercapacitors. *J. Power Sources* **2005**, *144*, 302–309. [[CrossRef](#)]
24. Teng, H.; Chang, Y.J.; Hsieh, C.T. Performance of electric double-layer capacitors using carbons prepared from phenol-formaldehyde resins by KOH etching. *Carbon* **2001**, *39*, 1981–1987. [[CrossRef](#)]
25. Cheng, F.; Yang, X.; Zhang, S.; Lu, W. Boosting the supercapacitor performances of activated carbon with carbon nanomaterials. *J. Power Sources* **2020**, *450*, 227678. [[CrossRef](#)]
26. Pekala, R.W.; Farmer, J.C.; Alviso, C.T.; Tran, T.D.; Mayer, S.T.; Miller, J.M.; Dunn, B. Carbon aerogels for electrochemical application. *J. Non-Cryst. Solids* **1998**, *225*, 74–80. [[CrossRef](#)]
27. Huang, C.W.; Wu, Y.T.; Hu, C.C.; Li, Y.Y. Textural and electrochemical characterization of porous carbon nanofibers as electrodes for supercapacitors. *J. Power Sources* **2007**, *172*, 460–467. [[CrossRef](#)]
28. Wang, K.; Wang, Y.; Hosono, E.; Zhou, H. Mesoporous carbon nanofibers for supercapacitor application. *J. Phys. Chem. C* **2009**, *113*, 1093–1097. [[CrossRef](#)]

29. Kim, E.S.; Lee, H.J.; Kim, B.H. Sandwich-structured carbon nanofiber/MnO₂/carbon nanofiber composites for high-performance supercapacitor. *Electrochim. Acta* **2022**, *406*, 139883. [[CrossRef](#)]
30. Zheng, J.-P.; Huang, J.; Jow, T.-R. The limitations of energy density for electrochemical capacitors. *J. Electrochem. Soc.* **1997**, *144*, 2026. [[CrossRef](#)]
31. Miller, J.-M.; Dunn, B.; Tran, T.-D.; Pekala, R.-W. Deposition of ruthenium nanoparticles on carbon aerogels for high energy density supercapacitor electrodes. *J. Electrochem. Soc.* **1997**, *144*, L309. [[CrossRef](#)]
32. González, A.; Goikolea, E.; Barrena, J.A.; Mysyk, R. Review on supercapacitors: Technologies and materials. *Renew. Sustain. Energy Rev.* **2016**, *58*, 1189–1206. [[CrossRef](#)]
33. Fang, B.; Binder, L. A novel carbon electrode material for highly improved EDLC performance. *J. Phys. Chem. B* **2006**, *110*, 7877–7882. [[CrossRef](#)] [[PubMed](#)]
34. Elisadiki, J.; Kibona, T.E.; Machunda, R.L.; Saleem, M.W.; Kim, W.-S.; Jande, Y.A.C. Biomass-based carbon electrode materials for capacitive deionization: A review. *Biomass Convers. Biorefinery* **2020**, *10*, 1327–1356. [[CrossRef](#)]
35. Zhang, B.; Kang, F.; Tarascon, J.M.; Kim, J.K. Recent advances in electrospun carbon nanofibers and their application in electrochemical energy storage. *Prog. Mater. Sci.* **2016**, *76*, 319–380. [[CrossRef](#)]
36. Zhang, L.; Huang, Y.; Zhang, Y.; Gu, H.; Fan, W.; Liu, T. Flexible Electrospun Carbon Nanofiber@NiS Core/Sheath Hybrid Membranes as Binder-Free Anodes for Highly Reversible Lithium Storage. *Adv. Mater. Interfaces* **2016**, *3*, 1500467. [[CrossRef](#)]
37. Zhang, L.; Aboagye, A.; Kelkar, A.; Lai, C.; Fong, H. A review: Carbon nanofibers from electrospun polyacrylonitrile and their applications. *J. Mater. Sci.* **2014**, *49*, 463–480. [[CrossRef](#)]
38. Yusof, N.; Ismail, A.F. Post spinning and pyrolysis processes of polyacrylonitrile (PAN)-based carbon fiber and activated carbon fiber: A review. *J. Anal. Appl. Pyrolysis* **2012**, *93*, 1–13. [[CrossRef](#)]
39. Kim, C.; Yang, K.S. Electrochemical properties of carbon nanofiber web as an electrode for supercapacitor prepared by electrospinning. *Appl. Phys. Lett.* **2003**, *83*, 1216–1218. [[CrossRef](#)]
40. Lee, H.M.; Kim, H.G.; Kang, S.J.; Park, S.J.; An, K.H.; Kim, B.J. Effects of pore structures on electrochemical behaviors of polyacrylonitrile (PAN)-based activated carbon nanofibers. *J. Ind. Eng. Chem.* **2015**, *21*, 736–740. [[CrossRef](#)]
41. Altin, Y.; Celik Bedeloglu, A. Polyacrylonitrile/polyvinylalcohol-based porous carbon nanofiber electrodes for supercapacitor applications. *Int. J. Energy Res.* **2021**, *45*, 16497–16510. [[CrossRef](#)]
42. Xu, W.; Xin, B.; Yang, X. Carbonization of electrospun polyacrylonitrile (PAN)/cellulose nanofibril (CNF) hybrid membranes and its mechanism. *Cellulose* **2020**, *27*, 3789–3804. [[CrossRef](#)]
43. Hu, H.; Hu, Z.; Ren, X.; Yang, Y.; Qiang, R.; An, N.; Wu, H. Non-Covalent Functionalization of Graphene with Bisphenol A for High-Performance Supercapacitors. *Chin. J. Chem.* **2015**, *33*, 199–206. [[CrossRef](#)]
44. Javaid, A.; Ho, K.K.C.; Bismarck, A.; Shaffer, M.S.P.; Steinke, J.H.G.; Greenhalgh, E.S. Multifunctional structural supercapacitors for electrical energy storage applications. *J. Compos. Mater.* **2014**, *48*, 1409–1416. [[CrossRef](#)]
45. Hao, W.; Waisi, B.I.; Vadas, T.M.; McCutcheon, J.R. Chemically activated carbon nanofibers for adsorptive removal of bisphenol-A: Batch adsorption and breakthrough curve study. *Chin. J. Chem. Eng.* **2023**, *61*, 248–259. [[CrossRef](#)]
46. Hulicova, D.; Oya, A. The polymer blend technique as a method for designing fine carbon materials. *Carbon* **2003**, *41*, 1443–1450. [[CrossRef](#)]
47. Wang, H.; Wang, W.; Wang, H.; Jin, X.; Niu, H.; Wang, H.; Zhou, H.; Lin, T. High Performance Supercapacitor electrode Materials from Electrospun Carbon Nanofibers in Situ Activated by High Decomposition Temperature Polymer. *ACS Appl. Energy Mater.* **2018**, *1*, 431–439. [[CrossRef](#)]
48. Yang, W.; Cao, L.; Li, W.; Du, X.; Lin, Z.; Zhang, P. Carbon Nanotube prepared by catalytic pyrolysis as the electrode for supercapacitors from polypropylene wasted face masks. *Ionics* **2022**, *28*, 3489–3500. [[CrossRef](#)] [[PubMed](#)]
49. Lu, Y.; Zhang, F.; Zhang, T.; Leng, K.; Zhang, L.; Yang, X.; Ma, Y.; Huang, Y.; Zhang, M.; Chen, Y. Synthesis and supercapacitor performance studies of N-doped graphene materials using o-phenylenediamine as the double-N precursor. *Carbon* **2013**, *63*, 508–516. [[CrossRef](#)]
50. Lee, K.S.; Seo, Y.J.; Jeong, H.T. Capacitive behavior of functionalized activated carbon-based all-solid-state supercapacitor. *Carbon Lett.* **2021**, *31*, 1041–1049. [[CrossRef](#)]
51. Tan, Y.; Lin, D.; Liu, C.; Wang, W.; Kang, L.; Ran, F. Carbon nanofibers prepared by electrospinning accompanied with phase-separation method for supercapacitors: Effect of thermal treatment temperature. *J. Mater. Res.* **2017**, *33*, 1120–1130. [[CrossRef](#)]
52. Musiol, P.; Szatkowski, P.; Gubernat, M.; Weselucha-Birczynska, A.; Blazewicz, S. Comparative study of the structure and microstructure of PAN-Based nano-and micro-carbon fibers. *Ceram. Int.* **2016**, *42*, 11603–11610. [[CrossRef](#)]
53. Deitzel, J.M.; Kleinmeyer, J.; Harris, D.E.A.; Tan, N.B. The effect of processing variables on the morphology of electrospun nanofibers and textiles. *Polymer* **2001**, *42*, 261–272. [[CrossRef](#)]
54. Grzyb, B.; Machnikowski, J.; Weber, J.V.; Koch, A.; Heintz, O. Mechanism of co-pyrolysis of coal-tar pitch with polyacrylonitrile. *J. Anal. Appl. Pyrolysis* **2003**, *67*, 77–93. [[CrossRef](#)]
55. Hantel, M.M.; Kaspar, T.; Nesper, R.; Wokaun, A.; Kötz, R. Partially reduced graphite oxide for supercapacitor electrodes: Effect of graphene layer spacing and huge specific capacitance. *Electrochem. Commun.* **2011**, *13*, 90–92. [[CrossRef](#)]
56. ElAchaby, M.; Essamlali, Y.; ElMiri, N.; Snik, A.; Abdelouahdi, K.; Fihri, A.; Zahouily, M.; Soly, A. Graphene oxide reinforced chitosan/polyvinylpyrrolidone polymer bio-nanocomposites. *J. Appl. Polym. Sci.* **2014**, *131*, 41042. [[CrossRef](#)]

57. Qiao, W.; Yoon, S.H.; Mochida, I. KOH activation of needle coke to develop activated carbons for high-performance EDLC. *Energy Fuels* **2006**, *20*, 1680–1684. [[CrossRef](#)]
58. Liu, W.; Yan, X.; Lang, J.; Xue, Q. Electrochemical behavior of graphene nanosheets in alkylimidazolium tetrafluoroborate ionic liquid electrolytes: Influences of organic solvents and the alkyl chains. *J. Mater. Chem.* **2011**, *21*, 13205–13212. [[CrossRef](#)]
59. Cai, J.; Niu, H.; Li, Z.; Du, Y.; Cizek, P.; Xie, Z.; Xiong, H.; Lin, T. High-Performance Supercapacitor Electrode Materials from Cellulose-Derived Carbon Nanofibers. *ACS Appl. Mater. Interfaces* **2015**, *7*, 14946–14953. [[CrossRef](#)]
60. Kim, B.M.; Kim, H.Y.; Ju, Y.W.; Shin, J. Influence of the perovskite $\text{La}_{0.8}\text{Sr}_{0.2}\text{Mn}_{0.5}\text{Co}_{0.5}\text{O}_{3-\delta}$ on the Electrochemical Performance of the Graphene-Based Supercapacitor. *Energies* **2020**, *13*, 3030. [[CrossRef](#)]

Disclaimer/Publisher’s Note: The statements, opinions and data contained in all publications are solely those of the individual author(s) and contributor(s) and not of MDPI and/or the editor(s). MDPI and/or the editor(s) disclaim responsibility for any injury to people or property resulting from any ideas, methods, instructions or products referred to in the content.